JOURNAL OF SPACECRAFT AND ROCKETS
Vol. 39, No. 3, May–June 2002

Comprehensive Numerical Study of Jet-Flow Impingement over Flat Plates

Junxiao Wu,* Lin Tang,† Edward A. Luke,‡ Xiao-Ling Tong,§ and Pasquale Cinnella¶
Mississippi State University, Mississippi State, Mississippi 39762

The present study attempts a numerical investigation of the complex flowfield that occurs when an underexpanded jet collides against a solid surface. Numerous examples of this problem can be found in the aerospace industry (e.g., rocket test stands, multistage separation). A simplified geometry, already employed in previous experimental inquiries, was chosen as a test case: an underexpanded, axisymmetric, air jet impinging on a flat plate at varied angles. The three-dimensional Navier–Stokes equations were solved by means of a second-order-accurate Roe-type algorithm with a generalized grid formulation. The computational domain includes the convergent–divergent nozzle and the external field. The numerical results show various jet-shock and shock-shock interactions and compare very well with experimental data, including shadowgraph pictures and both location and values of the peak pressures on the inclined plate. This investigation focused on performing a thorough comparison between experiments and simulations, thereby establishing some level of confidence in the accuracy and reliability of the numerical tool developed, CHEM. CHEM can accommodate more complicated and realistic geometries and physical conditions than those encountered in this study: with further refinement and validation it can be used for rocket plume and plume/solid surface interaction simulations, both on the ground and in flight.

Nomenclature

A_j	=	area of the jth face, m^2
C_i	=	ith cell number
e_0	=	gas total energy, J/kg
$\boldsymbol{i}, \boldsymbol{j}, \boldsymbol{k}$	=	unit vectors for a Cartesian frame of reference (x, y, z)
$\boldsymbol{n}$	=	unit vector normal to a control surface
PR	=	pressure ratio, p_e/p_a
p_a	=	ambient pressure, 101,325 Pa (1 atm)
p_c	=	chamber pressure, Pa
p_e	=	nozzle-exit pressure, Pa
$\boldsymbol{Q}$	=	conservative variables
$\boldsymbol{q}_p$	=	primitive variables
R_i	=	residual for cell i
R_N	=	nozzle-exit radius, m
S	=	boundary surface for a control volume
$\boldsymbol{S}$	=	inviscid flux vector in Navier–Stokes equations
$\boldsymbol{S}_v$	=	viscous flux vector in Navier–Stokes equations
s	=	distance from the axis measured up on the plate, m
T	=	temperature, K
u, v, w	=	gas velocity in $\boldsymbol{i}, \boldsymbol{j}, \boldsymbol{k}$ directions, respectively, m/s
$\boldsymbol{u}$	=	gas velocity vector, m/s
V	=	volume, m^3
$\boldsymbol{W}$	=	source term vector in Navier–Stokes equations
x, y, z	=	Cartesian body axes, m
δ_{ij}	=	Kronecker tensor
$\delta\boldsymbol{r}$	=	displacement vector
Θ	=	energy flux term in the energy transport equation, J/m^2 · s
λ	=	conduction coefficient, J/s · m · K
μ	=	viscosity coefficient, kg/s · m
ρ	=	density, kg/m^3
τ	=	stress tensor, kg/s^2 · m

Received 16 May 2001; revision received 23 September 2001; accepted for publication 3 October 2001.

*Postdoctoral Fellow, Engineering Research Center, P.O. Box 9627.
†Research Associate III, Engineering Research Center, P.O. Box 9627.
‡Assistant Professor, Department of Computer Science, P.O. Box 9627. Member AIAA.
§Research Assistant Professor, Engineering Research Center, P.O. Box 9627.
¶Associate Professor, Department of Aerospace Engineering, P.O. Box 9627. Senior Member AIAA.

Introduction

THERE have been numerous studies on supersonic impinging jets, mostly driven by industrial applications. The impingement of a supersonic jet on a flat plate, which is either perpendicular or inclined to the jet axis, occurs in the rocket test-stand environment, during launch, multistage separation, and lunar and planetary landing and takeoff, for example. The supersonic impinging flow is composed of both supersonic and subsonic regions, shock-shock interactions, and wall/jet boundary layers. Moreover, high-temperature effects and chemical reactions could be important in some regions of the flow behind some of the strong shock waves and in the boundary-layer regions. Overall, it is a great challenge to fully understand the physics of these flows and correctly predict the heat and pressure loads on the impinging plate.

Previous work has concentrated on experiment and limited theoretical analysis. Gummer and Hunt[1] conducted experimental and theoretical studies on the impingement region produced by directing a uniform, axisymmetric, supersonic air jet onto a large, flat plate. Using the polynomial approximation and integral relations method, they obtained good agreement with experiment at higher jet Mach numbers, but accuracy was much reduced at lower values. They also found that the flow pattern varies with nozzle-to-plate distances. Kalghatgi and Hunt[2] studied the phenomenon of stagnation bubbles and conditions under which they occur. Lamont and Hunt[3] then investigated how the plate inclination angle affects flow pattern and pressure load on the plate.

With recent advances in high-performance computing, numerical simulation of these complex impinging flowfields is now possible. Kitamura and Iwamoto[4] conducted a numerical simulation of supersonic impinging jets exhausting from a convergent nozzle, using a total-variation-diminishing-type finite difference code. Their results show good comparison with experiment and also captured flow separation bubbles at certain nozzle-to-plate distance. The present authors[5] also carried numerical studies of the impingement on the perpendicular plate, and they simulated and analyzed the shock structures with varied nozzle-to-plate distances. They showed that a stagnation bubble exists only for certain nozzle-to-plate distance cases because of the effects of shock-shock interactions. They also showed that high temperatures can have a significant effect on shock structures.

As a logical extension of the previous study, the present investigation is focused on the inclined jet impingement, which exhibits distinctive and more complex features than the perpendicular jet impingement.[6] The maximum pressure on the inclined plate can be several times larger than that on the perpendicular plate because of the complex shock-shock interactions present. Moreover, the stagnation bubble can disappear when the plate angle decreases. The study by Lamont and Hunt[3] presented extensive experimental measurements of impingement on inclined plate with varied angles, which will be compared with numerical simulations. The present investigation will also provide analysis and explanations of the complex shock structures, thanks to the availability of detailed simulations.

The overall goal of this study is to perform a thorough comparison between experiments and simulations, thereby establishing some level of confidence in the accuracy and reliability of the numerical tool developed, CHEM. The geometry and physical conditions employed in the experiments have been reproduced in the simulations (namely, the impinging plate is flat and the fluid is cold air). However, CHEM can accommodate more complicated and realistic geometries and physical conditions than those encountered in this study: with further refinement and validation it can be used for rocket plume and plume/solid surface interaction simulations, both on the ground and in flight.

Governing Equations

The governing equations are expressed in integral form for flow in an arbitrary control volume V, closed by a boundary S:

$$\frac{\partial}{\partial t}\int_V \boldsymbol{Q}\,\mathrm{d}V + \oint_S (\boldsymbol{S}-\boldsymbol{S}_v)\cdot\boldsymbol{n}\,\mathrm{d}S = \int_V \boldsymbol{W}\,\mathrm{d}V \tag{1}$$

The unit vector $\boldsymbol{n}$ is normal to the infinitesimal area $\mathrm{d}S$ and points outward.

When ideal-gas flow is considered, the vector $\boldsymbol{W}$ is not present, and $\boldsymbol{Q}=[\rho, \rho u, \rho v, \rho w, \rho e_0]^T$. Utilizing a Cartesian frame of reference (x, y, z) whose unit vectors are $\boldsymbol{i}$, $\boldsymbol{j}$, and $\boldsymbol{k}$, respectively, the flux vectors $\boldsymbol{S}$ and $\boldsymbol{S}_v$ read

$$\boldsymbol{S}=\begin{bmatrix}\rho\boldsymbol{u}\\ \rho u\boldsymbol{u}+p\boldsymbol{i}\\ \rho v\boldsymbol{u}+p\boldsymbol{j}\\ \rho w\boldsymbol{u}+p\boldsymbol{k}\\ \rho e_0\boldsymbol{u}+p\boldsymbol{u}\end{bmatrix},\qquad \boldsymbol{S}_v=\begin{bmatrix}0\\ \tau_{xx}\boldsymbol{i}+\tau_{xy}\boldsymbol{j}+\tau_{xz}\boldsymbol{k}\\ \tau_{yx}\boldsymbol{i}+\tau_{yy}\boldsymbol{j}+\tau_{yz}\boldsymbol{k}\\ \tau_{zx}\boldsymbol{i}+\tau_{zy}\boldsymbol{j}+\tau_{zz}\boldsymbol{k}\\ \Theta\end{bmatrix} \tag{2}$$

where

$$\Theta=(\tau_{xx}u+\tau_{yx}v+\tau_{zx}w)\boldsymbol{i}+(\tau_{xy}u+\tau_{yy}v+\tau_{zy}w)\boldsymbol{j} + (\tau_{xz}u+\tau_{yz}v+\tau_{zz}w)\boldsymbol{k}-\boldsymbol{q} \tag{3}$$

The pressure p is related to the conserved variables $\boldsymbol{Q}$ by means of the thermal equation of state. The stress-tensor components τ are expressed as

$$\tau_{ij}=\mu\left(\frac{\partial u_i}{\partial x_j}+\frac{\partial u_j}{\partial x_i}\right)-\frac{2}{3}\mu\nabla\cdot\boldsymbol{u}\delta_{ij},\qquad i,j=1,2,3 \tag{4}$$

The indices i and j refer to the x, y, and z space directions and velocity components. The heat flux vector $\boldsymbol{q}$ is modeled using Fourier's law:

$$\boldsymbol{q}=-\lambda\nabla T \tag{5}$$

The temperature T is related to the conserved variables $\boldsymbol{Q}$ by means of the caloric equation of state. The viscosity coefficient μ and conduction coefficient λ are usually evaluated by means of Sutherland's law, at least for temperatures lower than 1000 K.

Numerical Formulation

To perform a numerical simulation, the governing equations presented in the preceding section must be discretized. Here, the finite volume technique is used as the discretization approach, taking advantage of the integral form of the governing equations. The current formulation is designed to utilize hybrid (generalized) grids,[7] although the grids employed for now are structured. In the present study the cell-centered approach is used for storing the conserved variables and for the subsequent solution procedure. The cell-averaged flow variables at the cell centers are calculated as an integral average:

$$Q(C_i)=\frac{1}{V_i}\int_{V_i} Q(x,y,z)\,\mathrm{d}V \tag{6}$$

where V_i is the cell volume. Then, the governing equations [Eq. (1)] for a cell with volume V_i can be written as

$$\frac{\partial}{\partial t}\int_{V_i} Q_i\,\mathrm{d}V+\oint_{S_i}\boldsymbol{F}\cdot\boldsymbol{n}\,\mathrm{d}S=\int_{V_i}\boldsymbol{W}\,\mathrm{d}V \tag{7}$$

where $\boldsymbol{F}$ represents $\boldsymbol{S}-\boldsymbol{S}_v$ for simplicity.

A spatially discretized form of Eq. (7) is

$$\frac{\partial}{\partial t}\int_{V_i} Q_i\,\mathrm{d}V+\sum_{j=1}^{k_i}\boldsymbol{F}_{ij}\cdot\boldsymbol{n}_j A_j=\int_{V_i}\boldsymbol{W}\,\mathrm{d}V \tag{8}$$

In the preceding equation the indices i and j denote the cell and face numbers, respectively, and k_i is the total number of faces of the ith cell. The second term on the left-hand side of Eq. (8) represents the flux for the ith cell.

The inviscid flux crossing a cell face is calculated as the exact solution of an approximate Riemann problem.[8] The form suitable for chemically reacting flow problems has been developed by Cinnella[9] and is employed in the current study. To avoid numerical instability problems that sometimes accompany this family of schemes, an adaptive Riemann flux is employed, as suggested by Quirk.[10] This technique switches to a slightly more dissipative but stable Harten–Lax–van Leer–Einfeldt (HLLE) (see Ref. 11) scheme in regions near strong shocks. The HLLE flux is switched on for any cell within eight cells downstream of a sufficiently strong shock, using an iterative method appropriate for generalized grids. A strong shock is detected when the pressure jump across the shock exceeds a user-defined factor. (A value of three was used for this study, and it was found that the adaptive Riemann flux only plays a role in the highest pressure ratio impingement cases.) More details on this adaptive Riemann solver for generalized grids are given in Ref. 12.

A second-order scheme is used in the current simulations. The primitive flow variables $\boldsymbol{q}_p=[\rho, u, v, w, p]^T$ are assumed to be distributed linearly within each cell, and the linear distribution is reconstructed from the cell-averaged values. During the solution process, the flow variables at a cell face are extrapolated from the cell-averaged values using a linear reconstruction procedure.[13]

The piecewise linear reconstruction of the primitive variables is done using a Taylor-series expansion:

$$\boldsymbol{q}_p(x,y,z)=\boldsymbol{q}_p(x_i,y_i,z_i)+\nabla\boldsymbol{q}_p(x_i,y_i,z_i)\cdot\delta\boldsymbol{r}+\mathcal{O}[(\delta\boldsymbol{r})^2] \tag{9}$$

where $\nabla\boldsymbol{q}_p$ is the gradient of the primitive variables $\boldsymbol{q}_p$ and $\delta\boldsymbol{r}$ is the vector from the center of the cell (x_i, y_i, z_i) to the desired point (x, y, z). The gradient of $\boldsymbol{q}_p$ at the cell center is estimated using a least-squares technique that has been described elsewhere.[14] To remove nonphysical values near regions of high solution gradients and preserve monotonicity, a limiter function has to be applied to $\nabla\boldsymbol{q}_p$. The current study employs Venkatakrishnan's limiter.[15]

After discretization, the cell governing equations can be written as

$$\frac{\mathrm{d}}{\mathrm{d}t}Q_i=R_i \tag{10}$$

where the steady-state residual R_i is given by the expression

$$R_i = \frac{1}{V_i}\left(V_i W_i - \sum_{j=1}^{k_i} \boldsymbol{F}_{ij} \cdot \boldsymbol{n}_j A_j\right) \tag{11}$$

A backward Euler method is used for temporal discretization. The Newton method is employed to solve the nonlinear fully discretized equations, and the resulting linear system is solved using a symmetric Gauss–Seidel approach. The code CHEM has been developed to implement the preceding numerical schemes and has been recently validated.[5,16]

Geometry and Grids

The nozzle geometry used to produce both experimental and numerical results is a 15-deg half-angle, conical-type nozzle, as illustrated in Fig. 1. This nozzle consists of a circular contracting contour of 5.12 throat radii followed by a circular expansion contour of 2 throat radii. The throat radius is 10.7 mm with an exit radius of 15 mm.

The axisymmetric simulations are handled by building a "pie-slice" grid, formed by rotating a two-dimensional grid by 5 deg, forming one cell in the circumferential dimension, as illustrated in Fig. 2. Reflecting boundary conditions are used to enforce axisymmetry at the circumferential boundaries. For the cases where the plate angle departs from 90 deg, axisymmetry is lost, and a full three-dimensional grid is required (although a symmetry plane is used to reduce the problem size by a factor of two). For these cases a body of revolution (O-style) grid is used for coarse meshes, whereas an H-style grid is used to remove the centerline degeneracy for refined meshes, yielding more efficient and accurate solutions. As seen in Fig. 3, the grid degeneracy can frustrate numerical accuracy by unproductively packing cells near the axis; H-style grids correct this problem.

Boundary Conditions

A boundary condition is specified at the inlet of the nozzle, where pressure, velocity, and density are fixed. A slip boundary condition is used at the lip of nozzle, and an ambient coflow with Mach number 0.01 is introduced above the nozzle lip. Both slip and nonslip boundary conditions have been used for the nozzle wall: the shock structures are almost the same for the two different boundary conditions. A slip boundary condition is used on the plate when the plate is inclined to the jet plume because the viscosity should play little role when the bubble no longer exists, as shown in Ref. 3. A nonreflecting characteristic variable boundary condition is applied on the far-field boundary. As already mentioned, only half of the flowfield is simulated by exploiting symmetry.

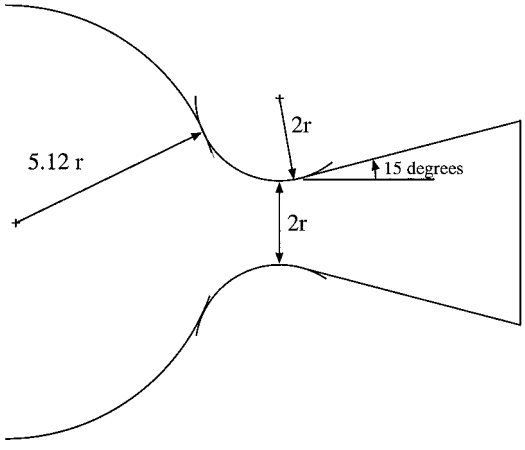

Fig. 1 Experimental nozzle geometry.

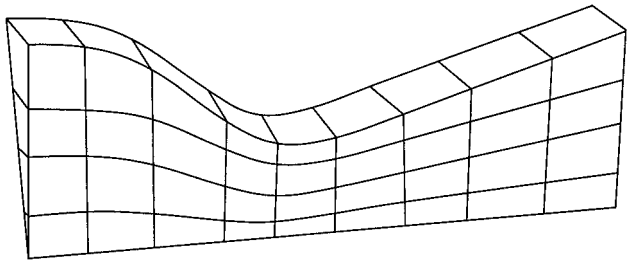

Fig. 2 Example nozzle grid for two-dimensional simulations.

Results and Discussion

For each class of impingement problem, several candidate cases were studied to determine grid convergence. In all cases we found that results on coarse grids matched well with finer grid solutions. In some cases, when the grid was sufficiently refined, it became difficult to obtain a steady-state solution. We attribute this problem to the fact that unsteady behavior was observed in the experimental results, as documented in Lamont and Hunt.[3] There are three principal sources of unsteadiness in these simulations: 1) a low-frequency oscillation (1–10 Hz), caused by the repeated formation and dispersal of a stagnation point recirculation bubble; 2) standing waves formed between the plate and any parallel surface, which can cause unsteadiness; and 3) large pressure fluctuations (caused by Hartmann resonance), caused by a reflection between the plate and the plate shock. In numerical simulations we have observed both sources 1 and 3. It is likely that the use of characteristic boundary conditions for the coflow region helps to prevent unsteadiness caused

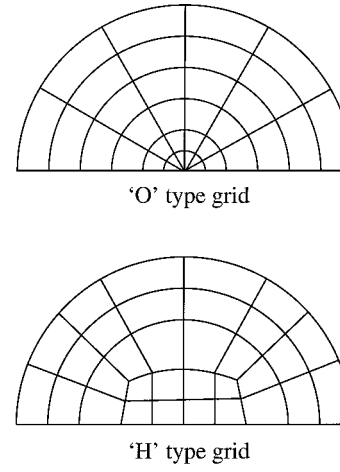

Fig. 3 Cross sections of three-dimensional grids.

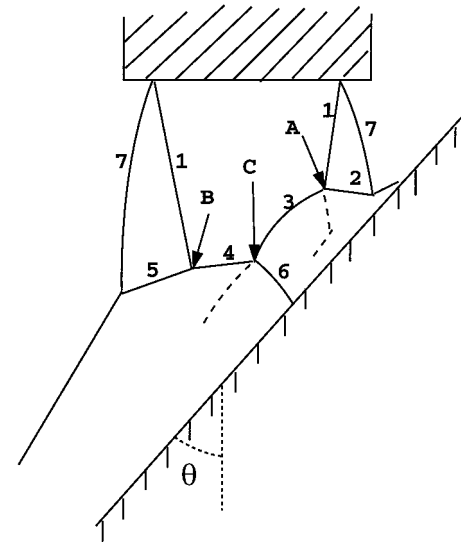

Fig. 4 Shock nomenclature: A, upper triple point; B, lower triple point; C, intermediate triple point; 1, jet shock; 2, upper-tail shock; 3, upper plate shock; 4, lower plate shock; 5, lower-tail shock; 6, intermediate-tail shock; and 7, jet edge. Also shown is plate angle θ (from Lamont and Hunt[3]).

by standing waves, as in source 2. To avoid unsteadiness in simulations, we selected grids sufficiently fine to resolve flow features but coarse enough to disperse unsteady modes of behavior. The appropriate grid was obtained from refinement studies for select cases.

In problems involving complex shock interactions, such as jet-impingement cases, it is difficult to ascertain when a steady-state solution is reached. Because of the nature of these problems, a slight variation in shock location can prevent numerical residuals from converging even after an effective steady-state solution has been reached. To identify these conditions, comparisons between shock structures over a course of hundreds of iterations is used. If the shock locations do not move after large numbers of iterations, the simulation is considered to be in steady state. This criterion was used for all of the results presented here.

The distance between nozzle exit and the center of the plate (z_{NP}) is chosen as $2.0D_N$ and $3.0D_N$, where D_N is the nozzle-exit diameter. The minimum and maximum of the angles θ that the plate makes with the nozzle are 30 and 90 deg, respectively. The cold air jet is channeled from a high-pressure reservoir into the atmosphere and impinges on the flat plate. The ratio PR between nozzle-exit pressure p_e and ambient pressure p_a is either 1.2 or 2.

To facilitate the discussion of current simulation results, Fig. 4 shows a sketch, taken from Lamont and Hunt,[3] explaining the nomenclature for the most common shock intersections. The following discussions will refer to this sketch. The numerical simulation results with different impingement distances and exit pressures obtained from CHEM will be analyzed and compared with experimental data.

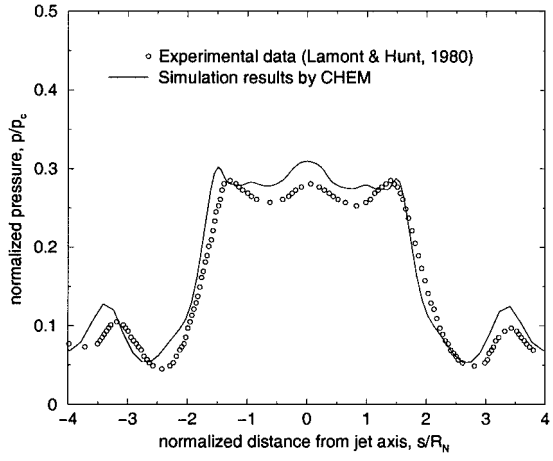

a) Plate angle = 90 deg

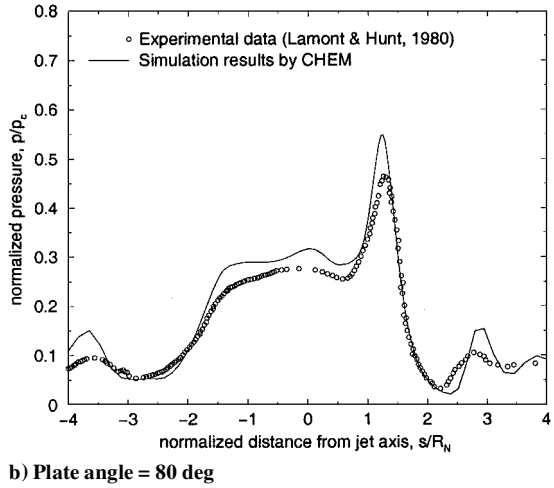

b) Plate angle = 80 deg

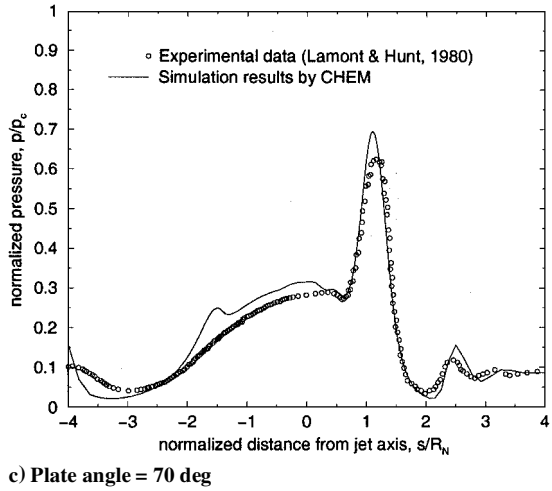

c) Plate angle = 70 deg

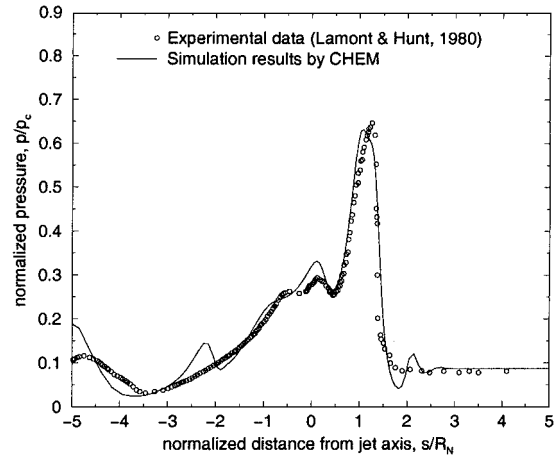

d) Plate angle = 55 deg

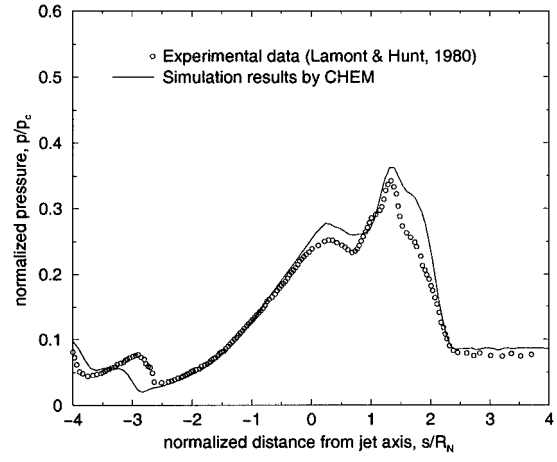

e) Plate angle = 35 deg

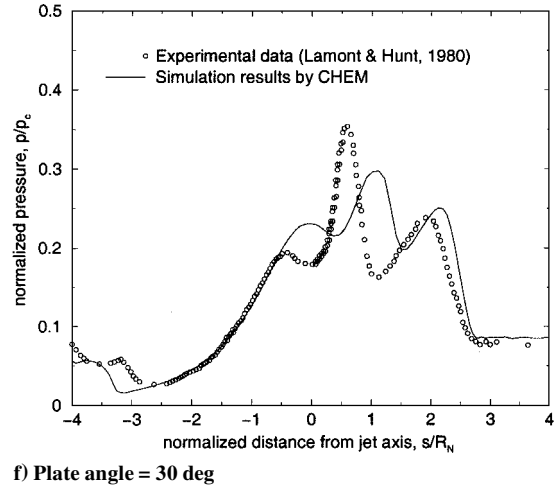

f) Plate angle = 30 deg

Fig. 5 Comparison of plate pressure distributions for $z_{NP} = 2D_N$ and $PR = 1.2$.

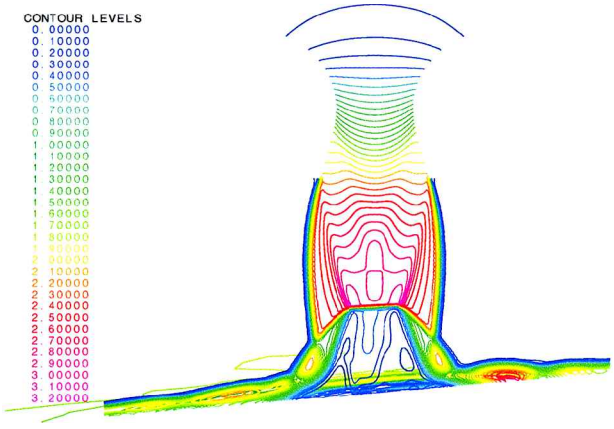

a) Plate angle = 85 deg

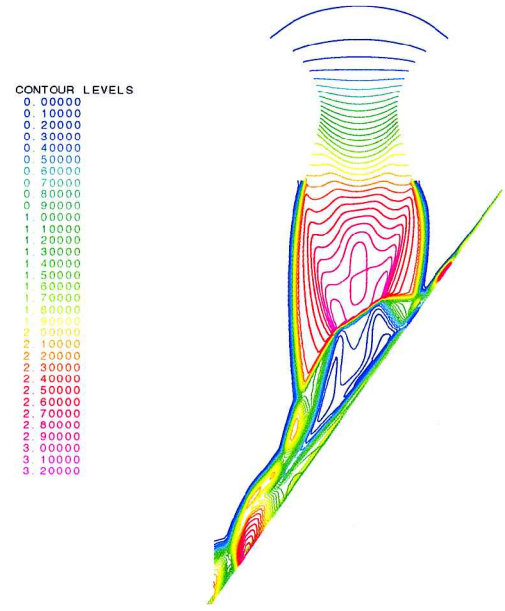

c) Plate angle = 35 deg

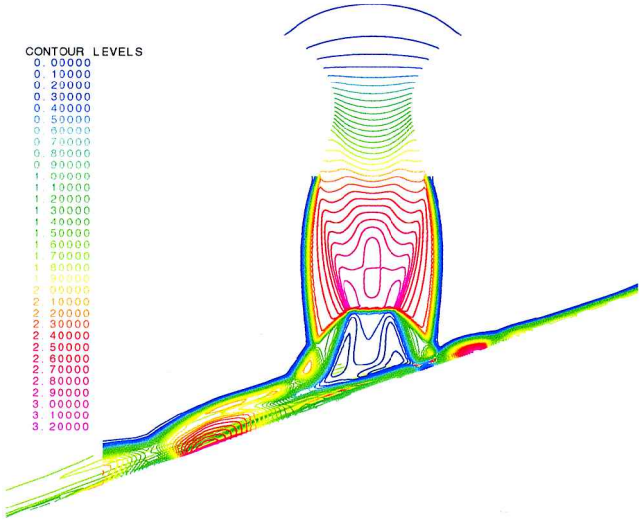

b) Plate angle = 70 deg

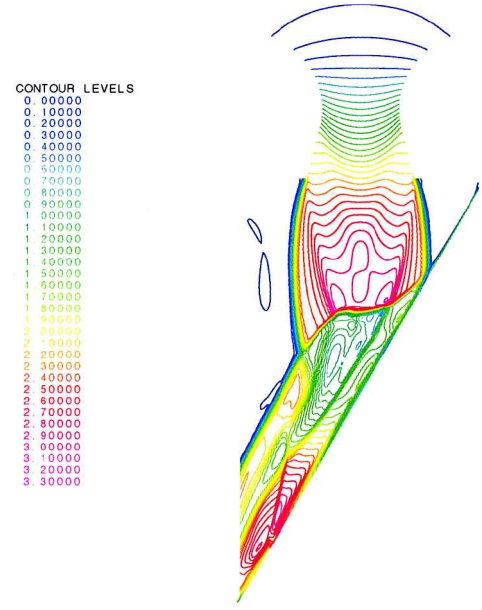

d) Plate angle = 30 deg

Fig. 6 Comparison of symmetry plate Mach-number contours for $z_{NP} = 2D_N$ and $PR = 1.2$.

For $z_{NP} = 2D_N$, $PR = 1.2$, the pressure distributions in the plane of symmetry are shown in Fig. 5 for various values of θ. Mach-number contours are shown in Fig. 6. Here and in the following, s is the distance from the jet axis measured along the plate. Overall, the agreement between present simulation and experimental data[3] is good. The discrepancy lies mainly in the peak pressure magnitude, probably as a result of insufficient grid resolution around the upper triple shock point.

At $\theta = 90$ deg, as analyzed by Wu et al.,[5] a recirculation bubble exists caused by the nozzle shocks, but by $\theta = 80$ deg (see Fig. 5b) the distribution of pressure has changed dramatically. The bubble has disappeared, and the peak pressure has increased to about $0.5p_c$, from the earlier value of $0.3p_c$. In general, the peak pressure occurs where the stagnation streamline intersects with the plane of symmetry. Thus from the location and the magnitude of the peak pressure, one can deduce at which side the stagnation streamline passes the upper-tail flow. Lamont and Hunt[3] have shown that the streamline passing through the intersection of the tail shock with the jet edge has a total pressure of $0.56p_c$, larger than the peak at $\theta = 80$ deg, which implies that the stagnation streamline passes away from the upper-tail flow. At $\theta = 70$ deg the peak pressure increases to $0.65p_c$, which implies that the stagnation streamline has moved into the upper-tail flow and originated a little away from the upper triple point and been brought to a subsonic value by a strong subtail plate shock. Decreasing θ to 60 deg, much remains the same, but the peak pressure increases to about $0.75p_c$.

The peak pressure decreases at $\theta = 55$ deg, and the shape of the pressure distributions remains unchanged until $\theta = 35$ deg, where a small hump starts to develop around the axis. From the reconstruction of the upper-tail flow at $\theta = 35$ deg using the Lockheed plume program,[3] it is concluded that a new triple point forms within the upper-tail shock, as a result of the interaction of a weak leading plate shock and a weak tail shock propagating from the upper triple point. The inner secondary tail flow turns into a supersonic jet embedded between two subsonic flows and causes the pressure hump around the axis.

At $\theta = 30$ deg, a new shock pattern occurs, as shown in the Mach contours at the plate of symmetry (compare Fig. 6d with Fig. 6c). The upper triple point has disappeared and has been replaced by a same-family confluence between the jet shock and the leading plate shock, these two combining into a weak upper plate shock, which then forms an intermediate triple point. The intermediate-tail

shock is propagated to the plate and results in the pressure peak at $s = 0.7R_N$.

A general point deduced from the preceding cases is that maximum pressure on an inclined plate can be considerably higher than that on a perpendicular plate: the largest pressure can be 70% above the perpendicular plate value. The main reason is the outside movement of the stagnation streamline into the upper-tail shock-flow region.

For cases $z_{NP} = 2D_N$, $PR = 2$, the comparison of the pressure distributions in the plane of symmetry are shown for various values of θ in Fig. 7, and Mach-number contours are depicted in Fig. 8. Overall, the agreement between present simulation and experimental data[3] is also good. The discrepancy lies mainly in the second maximum pressure magnitude (see in Figs. 7c and 7f), probably caused by insufficient grid resolution around the lower triple shock point.

As θ decreases, the changes in shock pattern follow the same sequence as for the $PR = 1.2$ cases: the stagnation streamline remains within the inner flow until $\theta = 70$ deg, when it moves to the upper-tail flow. The main differences occurs when $\theta = 30$ deg. The second peak has formed, and its location has moved to about $s = 0$ (downward from the location of the pressure hump in the $PR = 1.2$ case). This finding implies that the intermediate-tail shock has reached the plate earlier than the $PR = 1.2$ case, which seems reasonable,

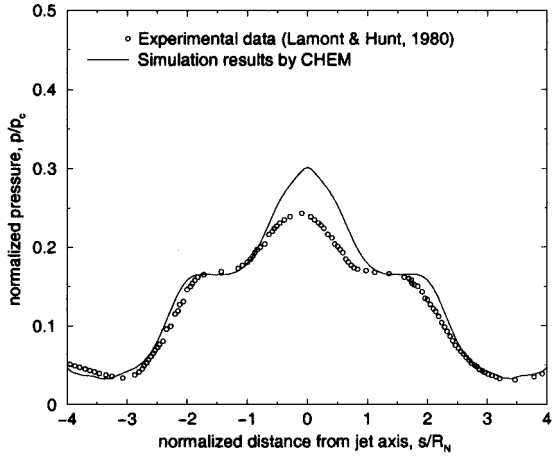

a) Plate angle = 90 deg

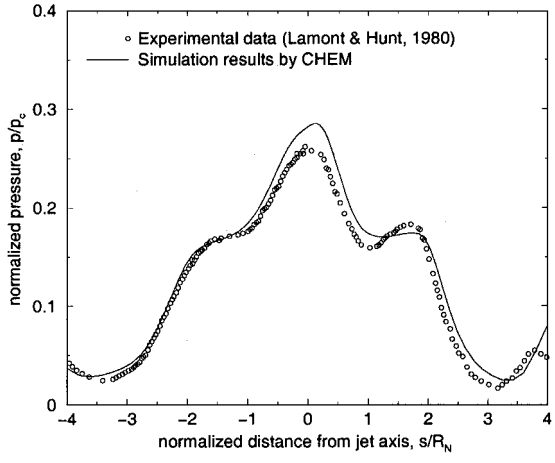

b) Plate angle = 80 deg

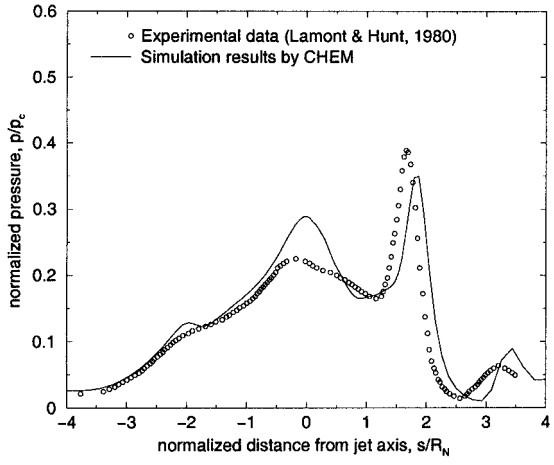

c) Plate angle = 70 deg

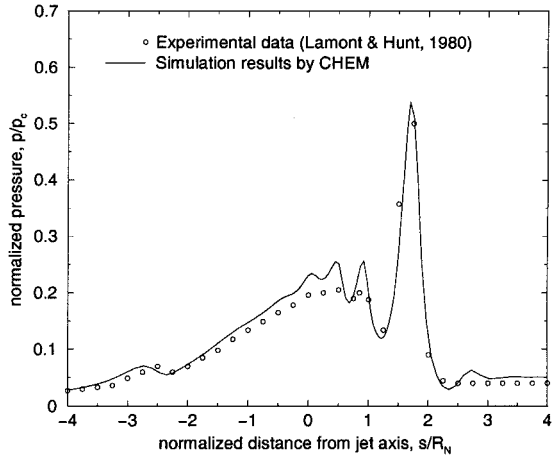

d) Plate angle = 55 deg

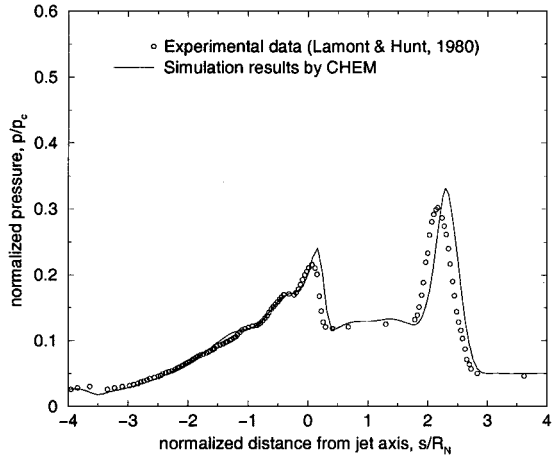

e) Plate angle = 35 deg

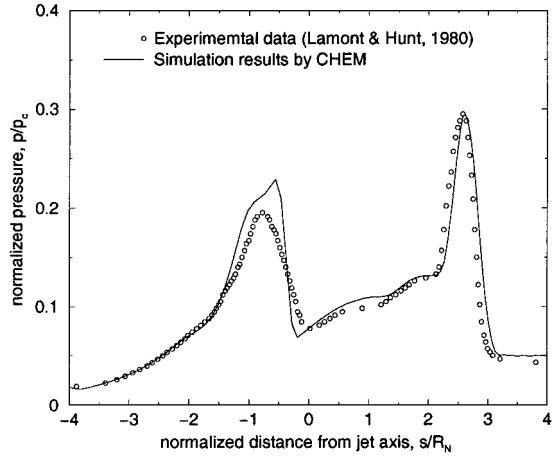

f) Plate angle = 30 deg

Fig. 7 Comparison of plate pressure distributions for $z_{NP} = 2D_N$ and $PR = 2$.

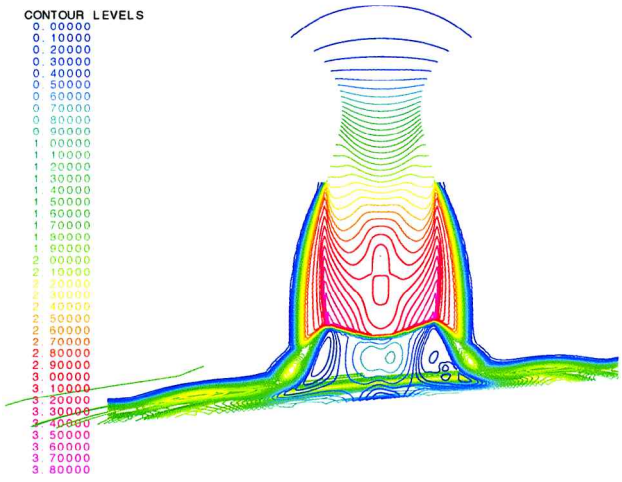

a) Plate angle = 85 deg

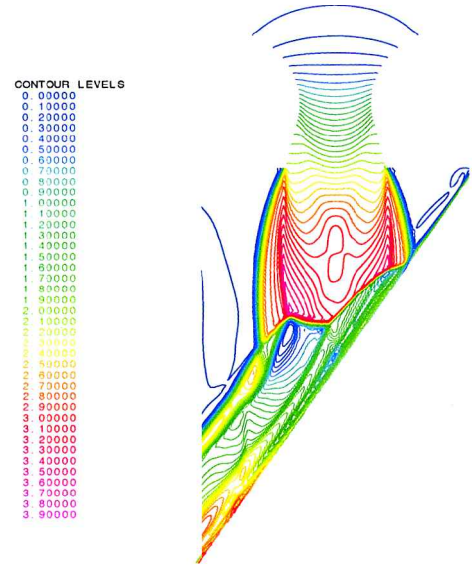

c) Plate angle = 35 deg

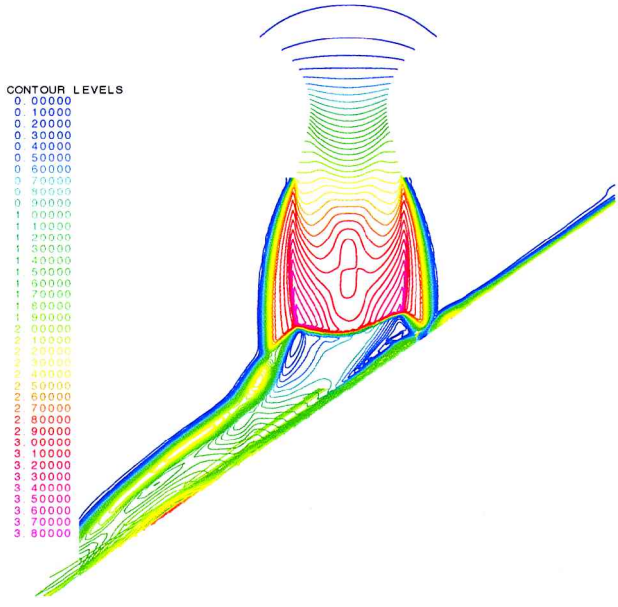

b) Plate angle = 55 deg

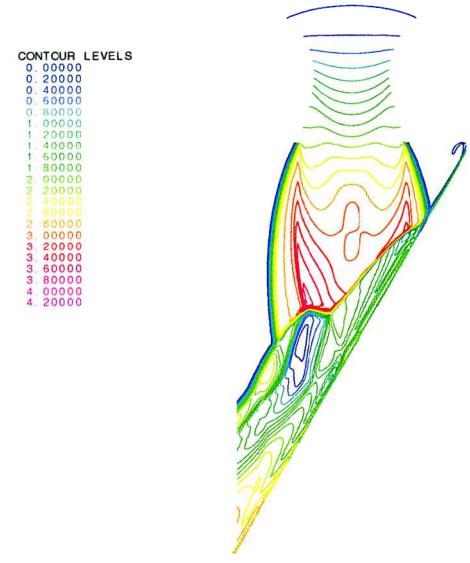

d) Plate angle = 30 deg

Fig. 8 Comparison of symmetry plate Mach-number contours for $z_{NP} = 2D_N$ and $PR = 2$.

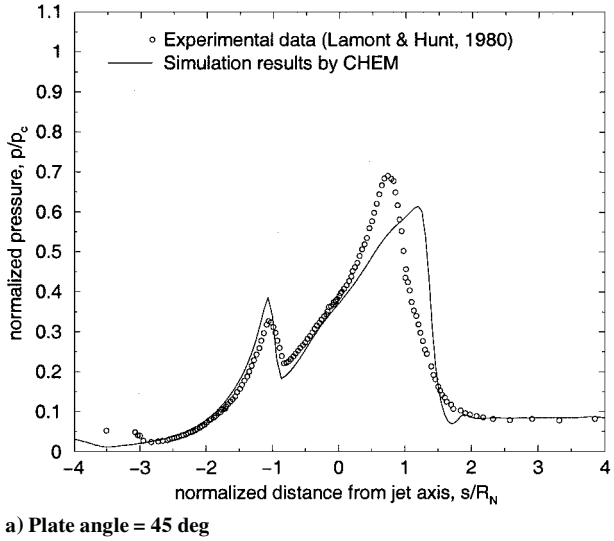

a) Plate angle = 45 deg

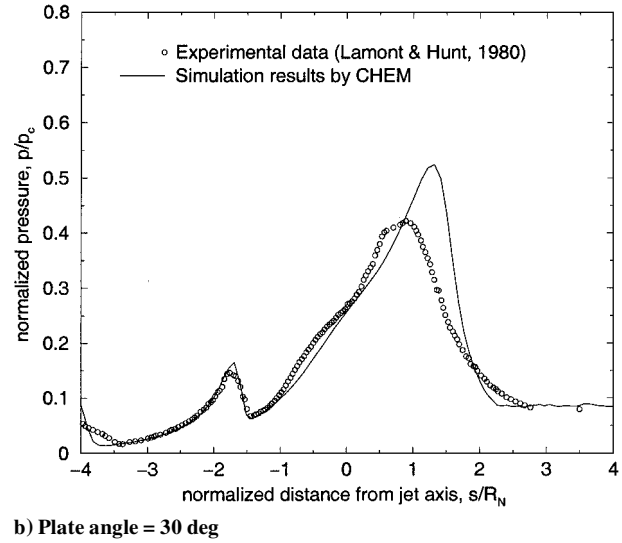

b) Plate angle = 30 deg

Fig. 9 Comparison of plate pressure distributions for $z_{NP} = 3D_N$ and $PR = 1.2$.

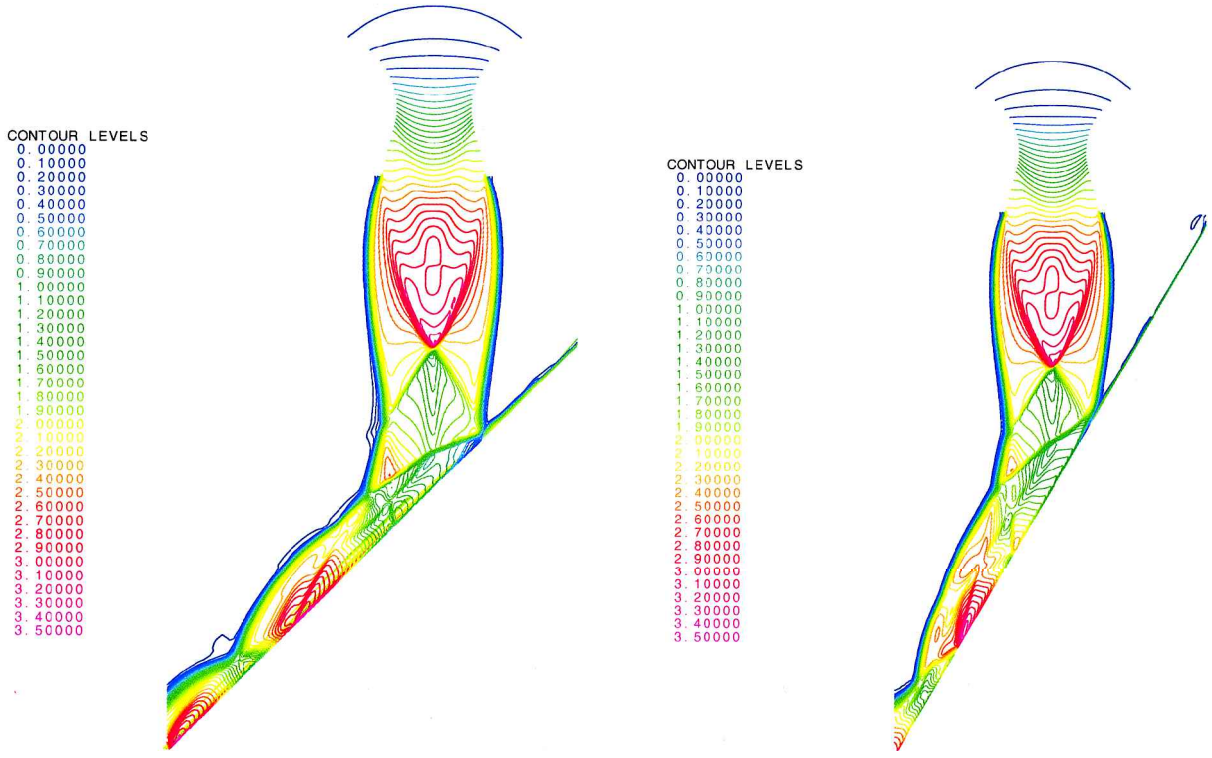

a) Plate angle = 45 deg **b) Plate angle = 30 deg**

Fig. 10 Comparison of symmetry plate Mach-number contours for $z_{NP} = 3D_N$ and $PR = 1.2$.

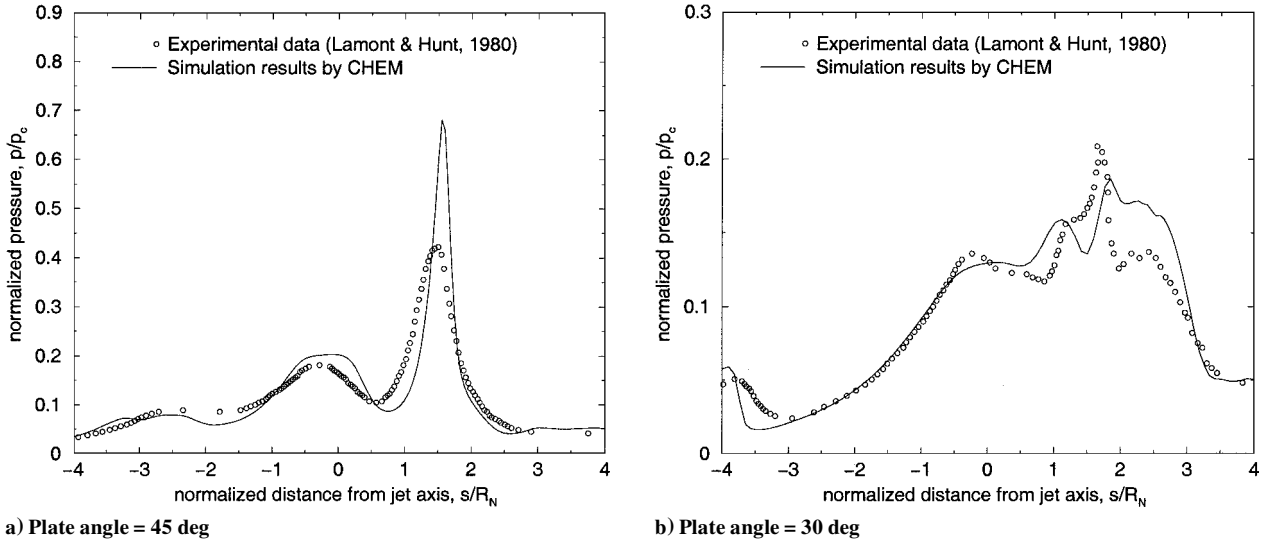

a) Plate angle = 45 deg **b) Plate angle = 30 deg**

Fig. 11 Comparison of plate pressure distributions for $z_{NP} = 3D_N$ and $PR = 2$.

because the shock in the higher-pressure case is much stronger than in the lower-pressure case. The Mach contour plots of the $PR = 2$ cases, shown in Figs. 8c and 8d, clearly show the shock structure difference from those of the $PR = 1.2$ cases.

For cases $z_{NP} = 3D_N$, $PR = 1.2$, the pressure distributions in the plane of symmetry are shown for only $\theta = 30$ and 45 deg in Fig. 9. Because of the higher computational cost for larger nozzle-to-plate distances, only these two cases have been studied. Overall, the agreement between present simulation and experimental data[3] is relatively good. The discrepancy between the CHEM simulation and experimental measurement lies in the first maximum pressure magnitude and location. The second maximum pressure, however, is matched very well. This implies that grid resolution should be increased to fully capture the flowfield around the upper triple point. The unsteadiness and boundary conditions may play a bigger role in the discrepancy as nozzle to plate distance increases.

In Fig. 9 the second peak pressure located around a negative s is an indication of a wave, which is the tail shock of a three-shock confluence point explained in Ref. 3. The good match around the second peak between the CHEM simulation and experimental measurement suggests that the shock structure of that region is well captured in the CHEM simulation.

The Mach contour plot of the $\theta = 45$ deg case in Fig. 10a shows that a Mach disk forms. In the preceding cases with $z_{NP} = 2D_N$, however, the plate was close enough to push the Mach disk upstream to form a plate shock instead.

For cases $z_{NP} = 3D_N$, $PR = 2$, the pressure distributions in the plane of symmetry are shown for $\theta = 30$ and 45 deg in Fig. 11. The simulation results for the $\theta = 45$ deg case show much higher peak value than the experimental data. From the Mach contour plot at $\theta = 45$ deg, shown in Fig. 12a, one can see that a secondary triple point occurs right below the upper triple point. The secondary triple

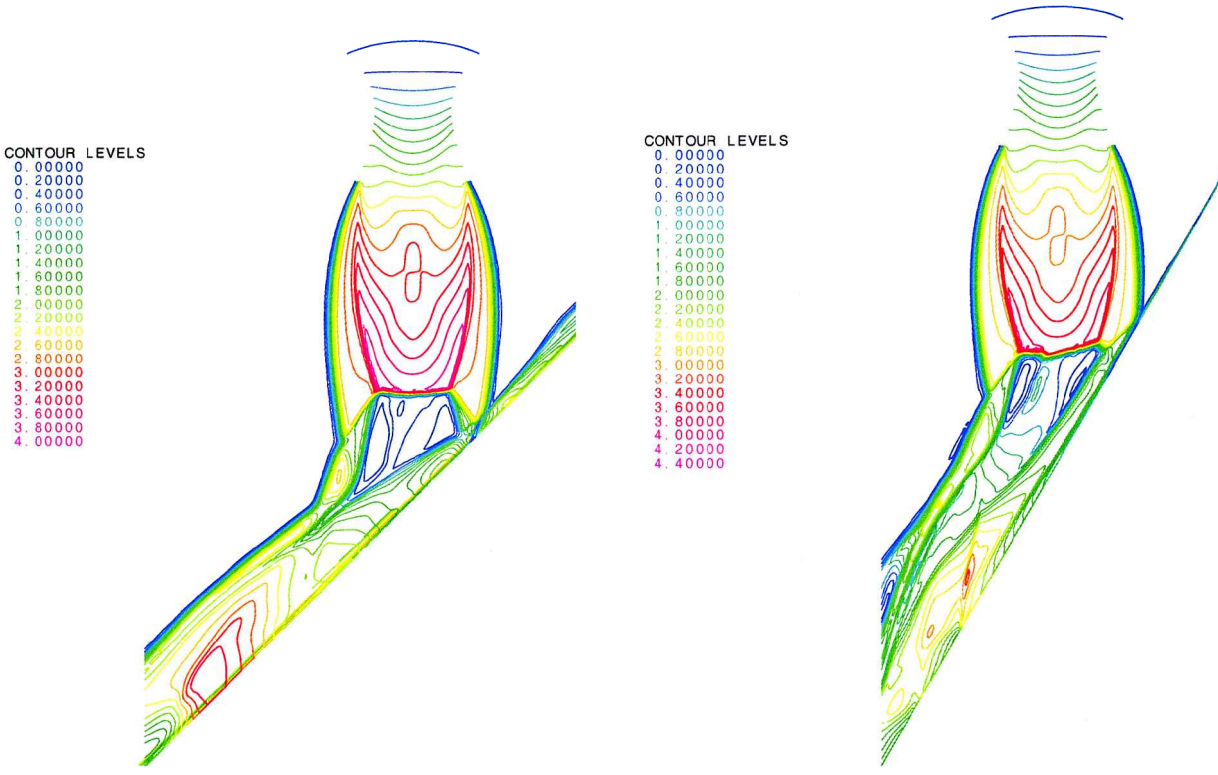

a) Plate angle = 45 deg **b) Plate angle = 30 deg**

Fig. 12 Comparison of symmetry plate Mach-number contours for $z_{NP} = 3D_N$ and $PR = 2$.

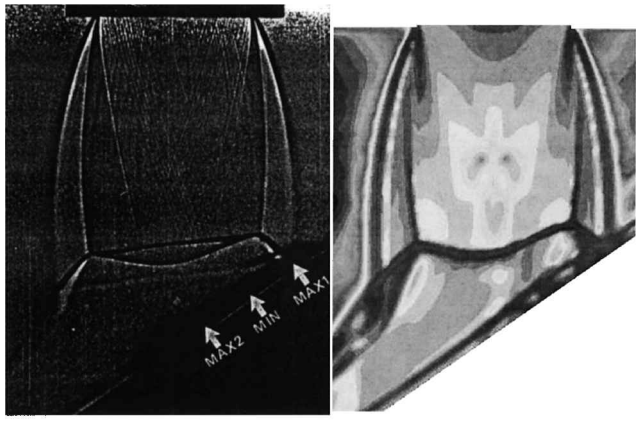

Experimental Shadowgraph **CHEM Simulation Results (Log of Density Gradients)**

Fig. 13 Comparison with experimental shadowgraphs by Lamont and Hunt[3]; $z_{NP} = 2D_N$, $PR = 2$, and plate angle = 55 deg. The CHEM simulation shadowgraph result is shown by plotting log of density gradients.

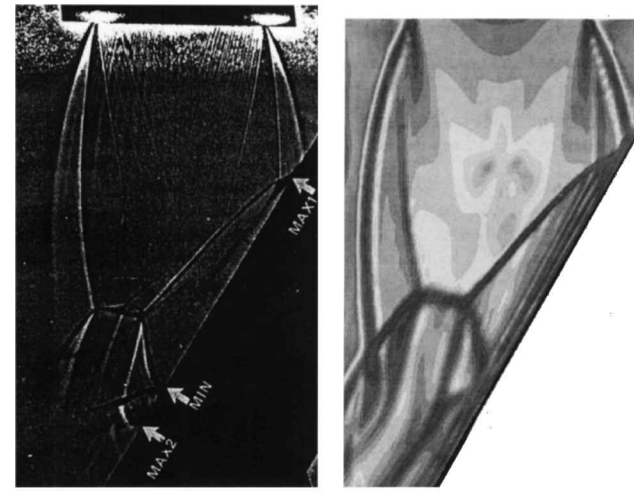

Experimental Shadowgraph **CHEM Simulation Results (Log of Density Gradient)**

Fig. 14 Comparison with experimental shadowgraphs by Lamont and Hunt[3]; $z_{NP} = 2D_N$, $PR = 2$, and plate angle = 30 deg. The CHEM simulation shadowgraph result is shown by plotting log of density gradients.

point is so close to the plate that it causes a very large pressure on the plate. The present simulation neglects viscosity effects, which is a valid assumption in most cases and saves computational cost, but when the triple point is very close to the plate viscosity might play a very important role in the pressure distribution on the plate and thus cause the large pressure discrepancy.

Figures 13 and 14 show a comparison on the symmetry plane between CHEM simulations and the experimental shadowgraphs for the cases $z_{NP} = 2D_N$, $PR = 2$, and plate angle $\theta = 55$ and 30 deg, respectively. The shock patterns and locations, including jet shock, upper triple point, lower triple point, plate shock, and lower plate shock, are all matched very well. The CHEM result is missing the straight shock line above the curved plane shock shown in the shadowgraph: the reason is that the shadowgraph is not a pure symmetry plane picture but a three-dimensional flowfield projection on the symmetry plane.

Conclusions

The numerical simulation of jet impingement with varied angles shows good agreement with experimental measurements in terms of plate pressure distribution. In general, the simulation results exhibit the same shock patterns as the experimental shadowgraphs.

As the jet impinges on an inclined plate, the creation of complex shock waves in the flow can cause one or two peak pressures on an inclined plate, their values exceeding those on a perpendicular plate by large amounts. A recirculation bubble sometimes is present in the 90-deg plate results, but it disappears as the plate becomes inclined to less than 85 deg. The flowfield is mainly shock dominated, although in certain cases, when the triple point is very close to the plate, viscosity can play an important role.

The current study has shown that the CHEM simulation results have been qualitatively consistent with experimental data and in many cases also in good quantitative agreement. With further refinement and validation CHEM can be used as a reliable tool for rocket plume and environment interaction studies.

Acknowledgments

This project has been supported by the NASA Stennis Space Center, with Peter Sulyma as Technical Monitor. The authors would like to thank Jeffrey West (currently at NASA Marshall Space Center) and Jody Woods for their help in reproducing the experimental data.

References

[1]Gummer, J. H., and Hunt, B. L., "The Impingement of a Uniform, Axisymmetric, Supersonic Jet on a Perpendicular Flat Plate," *Aeronautical Quarterly*, Vol. 22, No. 4, 1971, pp. 403–420.

[2]Kalghatgi, G. T., and Hunt, B. L., "Experiments on the Impingement of a Supersonic Jet on a Flat Plate," *Aeronautical Quarterly*, Vol. 27, No. 2, 1976, p. 169.

[3]Lamont, P. J., and Hunt, B. L., "The Impingement of Underexpanded, Axisymmetric Jets on Perpendicular and Inclined Flat Plates," *Journal of Fluid Mechanics*, Vol. 100, Pt. 3, 1980, pp. 471–521.

[4]Kitamura, S., and Iwamoto, J., "Numerical Analysis of Supersonic Impinging Jet," *Transactions of Japan Society for Aeronautical and Space Science*, Vol. 41, No. 132, 1998, pp. 57–64.

[5]Wu, J., Tang, L., Tong, X. L., Luke, E. A., and Cinnella, P., "Numerical Simulation of Under-Expanded Jet Impingement," *Developments in Theoretical and Applied Mechanics*, edited by H. V. Tippur and P. K. Raju, Vol. 20, College of Engineering, Auburn Univ., Auburn, AL, April 2000, pp. 174–181.

[6]Wu, J., Tang, L., Tong, X., Luke, E., and Cinnella, P., "Numerical Simulations of Jet Impingement and Jet Separation," Dept. of Aerospace Engineering, Mississippi State Univ., Rept. MSSU-ASE-00-2, Mississippi State, MS, Aug. 2000.

[7]Koomullil, R. P., and Soni, B. K., "Flow Simulation Using Generalized Static and Dynamic Grids," *AIAA Journal*, Vol. 37, No. 12, 1999, pp. 1551–1557.

[8]Roe, P. L., "Approximate Riemann Solvers, Parameter Vector, and Difference Schemes," *Journal of Computational Physics*, Vol. 43, May 1981, pp. 357–372.

[9]Cinnella, P., "Flux-Split Algorithms for Flows with Non-Equilibrium Chemistry and Thermodynamics," Ph.D. Dissertation, Dept. of Aerospace and Ocean Engineering, Virginia Polytechnic Inst. and State Univ., Blacksburg, VA, Dec. 1989.

[10]Quirk, J., "A Contribution to the Great Riemann Debate," Inst. for Computer Applications in Science and Engineering, Paper 92-64, Jan. 1992.

[11]Einfeldt, B., "On Godunov-Type Methods for Gas Dynamics," *SIAM Journal on Numerical Analysis*, Vol. 25, No. 2, 1988, pp. 294–318.

[12]Luke, E., Wu, J., Tong, X., Tang, L., and Cinnella, P., "A Novel Approach to Multi-Disciplinary Simulations—Step 1: Non-Equilibrium Flow Solver," Mississippi State Univ. Engineering Research Center, Rept. MSSU-COE-ERC-01-05, Mississippi State, MS, Dec. 2001.

[13]Barth, T. J., and Jespersen, D. C., "The Design and Application of Upwind Schemes on Unstructured Meshes," AIAA Paper 89-0366, Jan. 1989.

[14]Strang, W., Tomaro, R. F., and Grismer, M. J., "The Defining Methods of Cobalt60: A Parallel, Implicit, Unstructured Euler/Navier–Stokes Flow Solver," AIAA Paper 99-0789, Jan. 1999.

[15]Venkatakrishnan, V., "On the Accuracy of Limiters and Convergence to Steady State Solutions," AIAA Paper 93-0880, Jan. 1993.

[16]Luke, E. A., "A Rule-Base Specification System for Computational Fluid Dynamics," Ph.D. Dissertation, Mississippi State Univ., Mississippi State, MS, Sept. 1999.

R. M. Cummings
Associate Editor